51st AIAA Aerospace Sciences Meeting
7-10 Jan 2013, Grapevine, TX
AIAA-2013-0721

Aero-Optical Environment around Turrets at Forward-Viewing Angles

Nicholas De Lucca[1], Stanislav Gordeyev[2], Eric Jumper[3],
University of Notre Dame, Notre Dame, Indiana, 46545

and

Donald Wittich[4]
Air Force Research Laboratory, Directed Energy Directorate, Kirtland AFB, NM 87117

Aero-optical effects around the hemispheric turret at forward looking angles for azimuthal angles of 0°, 45° and 85° at the elevation angle of 45° were parametrically investigated for multiple turret geometries and flow conditions. 2D wavefronts were acquired with a 32x32 sub-aperture resolution at 25 kHz with global beam jitter and accelerometer measurements acquired simultaneously at 100 kHz. Turret geometry was varied between flat and conformal window and from full hemisphere-on-cylinder to hemisphere-only and a partially-protruding hemisphere. Incoming boundary layer was varied between δ/D = 3% and δ/D = 15% while freestream Mach number was 0.3-0.6. Time-averaged OPD_{RMS} was computed for each case along with dominant POD modes, corresponding energy content and the global jitter spectra. A slow, unsteady defocus operating at normalized frequency of ST < 0.1 was found to be the primary component of wavefront aberration for these angles. The strength and exact shape of the defocus was shown to depend on not only the turret geometry, but also the incoming boundary layer thickness. The boundary layer thickness was shown to more substantially affect the hemisphere-only and partially-protruding hemisphere turrets than the full turret, introducing an additional broad-band global tip/tilt component between ST = 1 to ST = 10. The unsteady defocus and tip/tilt introduced were hypothesized to be related to the necklace vortex and wake instabilities driving slow changes in the global pressure field.

I. Introduction

TURRETS are convenient mechanical platforms to send or receive a laser beam from an airborne platform, as they can easily point and track the beam. However, from aero-optical point of view, turrets create additional density fluctuations around them, causing beam deterioration and therefore laser-beam intensity reduction at the far-field [1,2]. Most of the aero-optical distortions happen when the beam traverses the aft quadrant of the turret, where the separated flow creates unsteady turbulent wake with coherent vertical structures. As a consequence, aero-optical aberrations in the aft quadrant have been extensively studied in the last few years [1-6]

The forward-viewing angles, on the other hand, have been studied relatively less extensively and primarily for steady-lensing effects, see [1] and references therein. One reason is that the flow is attached over the most portion of the turret at forward-looking angles, resulting mostly only in steady-lensing aberrations. But recent computational simulations over different turrets [7] and experimental aero-optical measurements around flat-window turrets at side-looking angles [8] had suggested that the presence of the necklace vortex at the bottom of the turret and a slope discontinuity around a flat-window aperture create additional unsteadiness in the flow over turrets at forward-looking angles. Thus, there is a need to experimentally investigate how these flow features effect aero-optical distortions imposed on the beam at these forward-looking viewing angles.

[1] Graduate Student, Department of Mechanical and Aerospace Engineering, Hessert Laboratory for Aerospace Research, Notre Dame, IN 46556, Student Member.
[2] Research Associate Professor, Department of Mechanical and Aerospace Engineering, Hessert Laboratory for Aerospace Research, Notre Dame, IN 46556, Senior AIAA Member.
[3] Professor, Department of Mechanical and Aerospace Engineering, Hessert Laboratory for Aerospace Research, Notre Dame, IN 46556, AIAA Fellow.
[4] Aerospace Engineer, Laser Division, 3550 Aberdeen Ave SE.

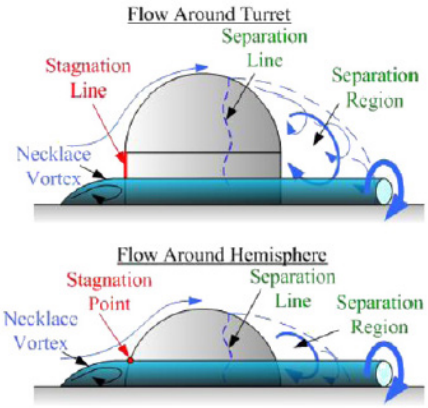

Figure 1. Flow structures over a hemisphere-on-cylinder turret and hemisphere-only turret, from [1].

The common features of a flow field around a turret are given in Figure 1. Around the base of the turret a necklace vortex forms below the stagnation point and extends downstream. The flow over the upstream portion of the turret remains attached, and from a turbulence-perspective, it is quiet and well-behaved. Downstream, the adverse pressure gradient eventually forces separation to occur and the turbulent wake to form. The same structures exist over the hemisphere-only turret, as also shown in Figure 1, and the same is true for a submerged hemisphere, though it isn't shown in Figure 1. Changing the height of the turret impacts the size and strength of the wake and necklace vortex [7]. Additionally, for Mach numbers typically larger than 0.55, a shock forms over the top of the turret; this has been shown to affect the aero-optical performance at specific looking-back angles [9, 10]. This paper focuses solely on side-looking and forward looking angles, additional information of the aero-optical behavior of turrets at back looking angles is available in [3,5].

II. Experimental Set-Up

Comprehensive series of tunnel tests to collect space- and time-resolved wavefronts around different turrets were conducted at the forward-looking quadrant. The tests were conducted in the White Field test facility at the University of Notre Dame. The basic turret used for this study was a hemisphere-on-cylinder turret with the turret diameter of D = 12 inches. In order to utilize the double-path optical approach, which will be described later, the turret was instrumented with an optical canister with either a flat aperture or a conformal-lens aperture. The latter one was designed to match the hemispherical curvature, but to work as an optical flat when the collimated beam hits it co-axially, see Figure 2 for schematics. The hemispherical portion of the turret with either the flat- or the conformal-aperture can be rotated to any elevation angle between 0 and 90 degrees and the turret assembly can be rotated to any azimuthal angle.

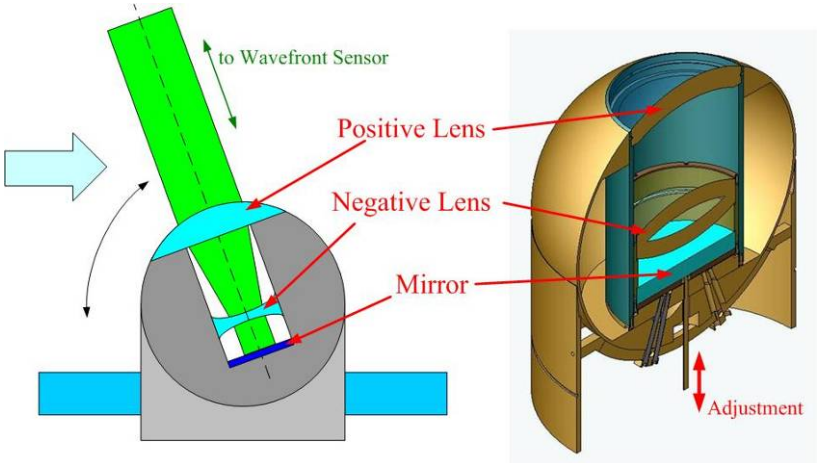

Figure 2. Optical canister for the conformal-aperture turret.

The schematic of the optical set-up is shown in Figure 3. A laser beam was expanded to a 4-inch collimated beam and was forwarded into the test section, where it was reflected normally from the flat- or the conformal-aperture on the turret, returning back to the optical table exactly along the same path it came into the test section, so-called a double-pass set-up. After returning to the optical table, the beam was split into two beams. One beam, after passing through a focusing lens, was directed to a Position Sensing Device (PSD) to measure the global jitter imposed on the returning beam. The second beam was forwarded on a high-speed wavefront sensor to measure higher-order wavefronts. The wavefront sensor was a Shack-Hartmann-type sensor with a 33 x 33 lenslet array. Wavefronts were taken at 25 kHz for 0.6 seconds, resulting in 15,000 wavefronts per run. In addition, four accelerometers were placed on the back of the optical canister in a non-collinear fashion such that both translational and rotational motions of the turret were measured. Accelerometer and global jitter data were collected simultaneously at 100 kHz for 15 seconds. Both the wavefront sensor and the jitter/accelerometers system were triggered to start collecting data at the same time to ensure that they observed the same flow conditions.

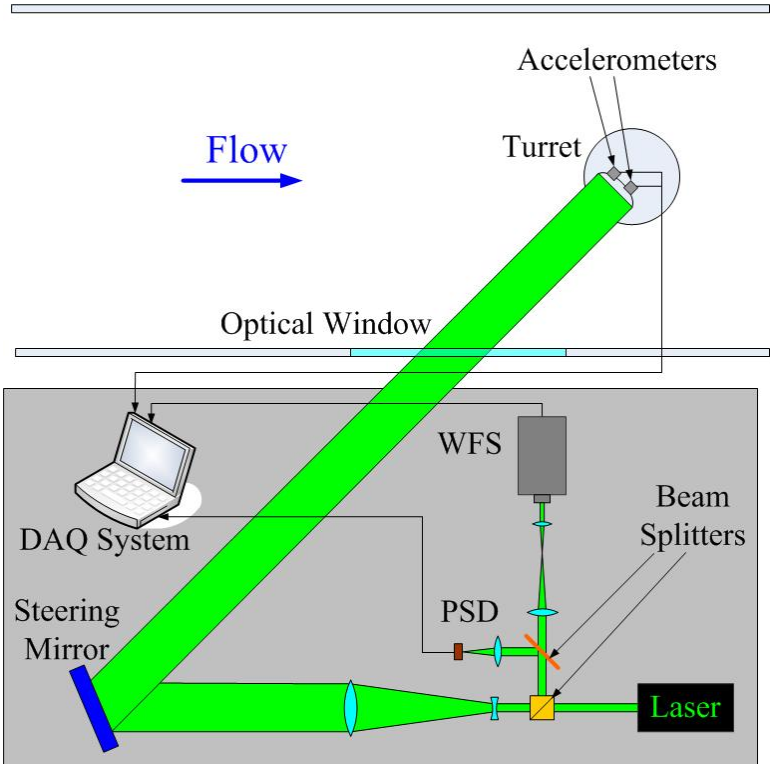

Figure 3. Schematics of the optical set-up.

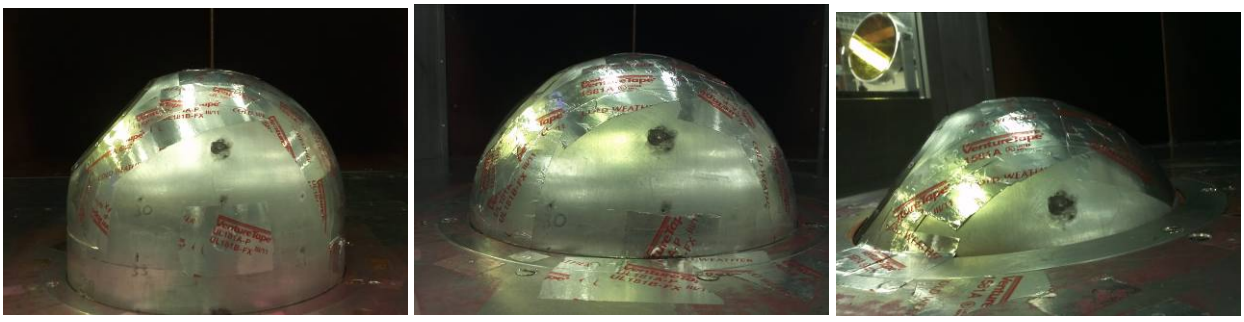

Figure 4. Tested turret geometries with a flat-aperture: a full turret (left), a hemisphere (middle) and a partially-protruding hemisphere (right).

Aero-optical data were collected for both conformal- and flat-aperture turrets with 3 different heights: a full turret with the cylinder height of 4 inches, resulting in the overall turret height of 10 inches, a hemisphere only with an overall height of 6 inches, and a partially-protruding hemisphere, when the hemisphere was penetrating the flow

by approximately 4.5 inches. Pictures of turrets with different heights are shown in Figure 4. Measurements were collected for a fixed elevation angle of 45 degrees for azimuthal angles of 0, 45 and 85 degrees for M = 0.3 and 0.4, with additional measurements at M = 0.5 and 0.6 for the partially-protruding hemisphere only. The incoming boundary layer was tripped by placing spanwise square bars of different sizes 4 feet upstream of the turret to increase incoming BL thickness. Three BL cases were tested: a thin BL with δ/D = 3%, a medium BL with δ/D = 7%, and a thick BL with δ/D = 15%.

III. Data Reduction

A. Wavefront data reduction

For every measured case, a steady component, time-dependent tip/tilt and piston were removed from each wavefront. The removed tip/tilt was not analyzed, as the global jitter was measured directly using a PSD. This instantaneous wavefront is the conjugate of the OPD, $W(x,y,t) = -OPD(x,y,t)$. To analyze the instantaneous magnitude of the spatial variation in each wavefront, the $OPD_{RMS}(t)$ was computed by taking the spatial RMS of the wavefront over the aperture, $OPD_{RMS}(t) = \langle W(x,y,t)^2 \rangle_{x,y}$. The temporal mean of this value, $\overline{OPD_{RMS}}$, later called OPDrms for simplicity, gives the time-averaged amount of aero-optical distortions over the aperture. As wavefronts are functions of time and space, temporal variance of wavefronts for all spatial points over the aperture was also calculated, $OPD_{RMS}(x,y) = \overline{W(x,y,t)^2}$. This quantity is useful in identifying the sections of the turret aperture that observe the largest aberrations. Again, for simplicity, it will be called as the spatial distribution of OPDrms. Both OPDrms and the spatial distribution of OPDrms provide important statistics about aero-optical distortions over the aperture. In selected cases Proper Orthogonal Decomposition (POD) was used to decompose wavefronts into spatial modes and their temporal coefficients.

All aero-optical results are normalized by $(\rho/\rho_{SL})M^2D$, where ρ is the free stream density and ρ_{SL} is the density at sea level. This scaling was previously shown to correctly normalize aero-optical distortions over turrets for subsonic Mach numbers less than 0.5 assuming Re_D is above some critical value [1]. All frequencies are normalized by the incoming speed and the turret diameter, $ST = fD/U_\infty$,

B. Wavefront Proper Orthogonal Decomposition

Proper Orthogonal Decomposition (POD), commonly referred to as Karhunen–Loève Decomposition or principle component analysis, was used to obtain the modes and energy content of the instantaneous 2D wavefronts. The POD modes are obtained by computing the eigenvectors of the covariance matrix of the wavefronts, $R(x,y,x',y')\varphi_i(x',y') = \lambda\varphi(x,y)$. Here, the covariance matrix, R, is given by $R(x,y,x',y') = \overline{W(x,y,t)W(x',y',t)}$. The average energy in each mode is given by the corresponding eigenvalue, λ_i. POD modes are generated as the optimal orthogonal basis; in other words, the energy in each mode is maximized such that the system can be represented by the fewest modes possible. This technique has been applied previously to analyze the primary modes in 2D wavefronts taken on the Airborne Aero-Optics Laboratory [11].

C. Jitter Reduction

To separate the mechanical and aero-optical jitter components, the linear stochastic estimation (LSE) technique, developed by Adrian [12] was employed. This technique generates an estimate of a measured quantity using a set of other measured quantities. It does this using the correlation between a quantity to be estimated and the additional measured quantities through the cross correlation tensor of the additional quantities. Details of the technique can be found in [5]. This technique was used to generate an estimation of the mechanically-induced part of the global jitter data, using a linear sum of the accelerometer data which was then subtracted from the original signal. Figure 4 shows the example of the LSE-based technique. Using the technique, the jitter spectra were split into the two different components. The measured overall jitter spectra, $\hat{\Theta}(f)$, consists of both the

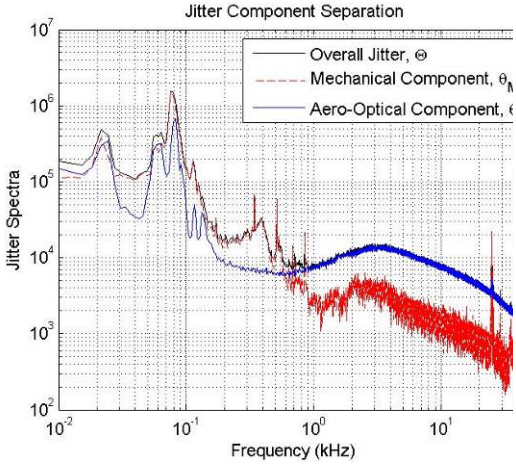

Figure 5: Example of jitter spectrum separation using LSE technique.

mechanically-induced jitter component, $\hat{\theta}_M(f)$, and the aero-optical component, $\hat{\theta}(f)$. The LSE reconstruction approximates the mechanically-induced component, $\theta_M \approx \tilde{x}_i$ by cross-correlating the accelerometers' spectra to the overall jitter and the aero-optical component was estimated as $\theta = \Theta - \theta_M \approx \Theta - \tilde{x}_i$. At frequencies above 600 Hz, the correlation with the mechanically induced jitter spectrum falls off very rapidly and aero-optical effects dominate at higher frequencies. Below 100 Hz, the largest contributors are from non-aero-optical effects. These include the vibration of the optical table or optical components such as mirrors and lenses and the vibration of the tunnel windows. Power spectra for the global spectra were calculated for all measured angles and Mach numbers.

IV. Wavefront Results

A. Angular dependence for different turrets

Time-averaged OPDrms for different turret heights and aperture geometry as a function of the azimuthal angle for a thin incoming BL are presented in Figure 6. The incoming $M = 0.4$. The aero-optical distortions are the largest for the forward-looking angle of 0 degrees; for the conformal-aperture turret distortions monotonically decrease with the azimuthal angle increasing, so for the side-looking angle of 85 degrees aberrations are at minimum. The flat-aperture introduces an additional complexity for side-looking angles of 45 and 85 degrees, where the flow is tripped by the upstream slope discontinuity between the turret surface and the aperture and, although the flow quickly re-attaches over the aperture, the increased turbulence levels of the re-attached flow cause larger aero-optical effects, compared to the conformal-aperture results. In general, the partially-protruding hemisphere is aero-optically less disturbing that the full turret.

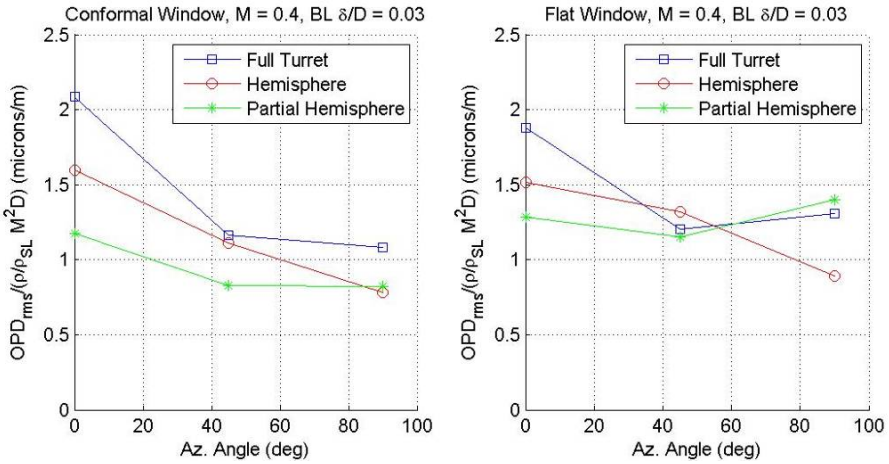

Figure 6. Normalized OPDrms for different turret heights with conformal (left plot) and flat (right plot) apertures at different azimuthal angles. The incoming M = 0.4, the incoming BL δ/D=0.03.

The fact that the aero-optical aberrations are the largest for looking directly forward is somewhat surprising, as usually it is assumed that the flow is attached over the aperture for forward-looking angles, resulting only in steady-lensing aberrations and temporal variation of the wavefronts are relatively small; but in fact the measured OPDrms for the forward-looking angle of zero degrees are comparable with levels of aero-optical distortions observed at back-looking angles [3], where the flow is separated and forms a turbulent wake. To understand the nature of the aero-optical distortions at the looking-forward angle, wavefronts were decomposed into a sum of spatial POD modes, multiplied by temporal coefficients. The first two POD modes for the full turret with the conformal aperture for M = 0.4 are presented in Figure 7, top plot. The first mode represents primarily a stationary vertical defocus, with the relative amount of optical energy captured by this spatial mode at approximately 50 percent. The second mode shows a stationary defocus predominantly in the horizontal plane and captures about 24% of the optical energy. The spectra of the temporal coefficients for the first two modes are given in Figure 7, bottom plot, and revealed the low-frequency, below ST = 0.2, nature of the aberrations. So, wavefronts for the forward-looking angle are dominated by stationary and slowly changing-in-time defocus; this is in contrast with wavefronts for back-looking angles, which are dominated by fast-moving, compact components caused by traveling vortical structures in the separated shear layer. The most probable sources of these looking-forward distortions are the slowly-changing

necklace vortex formed upstream of the turret and fluctuations in the wake of the turret. The slowly-varying necklace vortex displaces the flow, which effectively changes a fluidic shape of the turret, and consequently imposes low-frequency changes on the global pressure and density fields around the forward portion of the turret via Biot-Savart induction, resulting in low-frequency variations of the wavefronts. Fluctuations of the wake will similarly change the turret's fluidic shape and cause low frequency changes in the density and pressure fields. Thus, while amplitudes of the aero-optical distortions for forward-looking angles are relatively large, it is dominated by low-spatial, slow-varying modes, which can be fixed by a conventional adaptive-optics system.

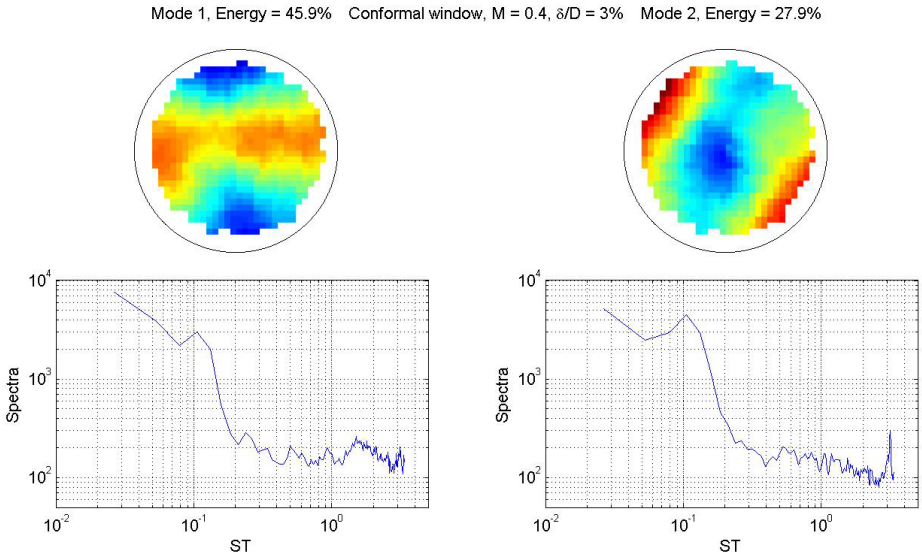

Figure 7. Top: First two dominant spatial POD modes for the full turret with the conformal aperture, azimuthal angle is 0 degrees, M = 0.4, δ/D = 0.03. Bottom: amplitude spectra of the temporal coefficients for these POD modes.

Figure 8, gives the same information as Figure 7, except for the flat window instead of the conformal one. The spectra for the temporal coefficients of the first two modes, Figure 8 bottom, are very similar to those of the conformal window turret. This shows that the two dominant modes do not experience a change in frequency content when changing window geometry. However, from Figure 8, Top, the order of the two modes is switched. The flat window aberrations have larger energy content in the horizontal defocus mode than in the vertical mode. The sum of total energy content between these two defocus modes is approximately the same for both cases, but 9% of the total optical energy is shifted from the second mode into the first for the flat window case. This modal shift demonstrates that the flat window has a substantial effect on the relative importance of these two defocus modes to the aero-optical distortions observed at this angle. However, as will be shown later, the difference in the total amount of optical aberrations between the two windows is small, so it doesn't reduce the sum total of unsteady defocus.

The slowly-changing defocus creates a specific spatial distribution of OPDrms, with an increased level of OPDrms near the middle of the aperture and near the edge of the aperture and reduced levels of OPD half-way between the center and the edge of the aperture. Spatial distribution of OPDrms for the azimuthal angle of 0 degrees for different aperture types and turret heights are presented in Figure 9. The unsteady defocus is the strongest for the full turret, see left column in Figure 9, it becomes small for the hemisphere, shown in middle column in Figure 9 and goes even smaller for the partially-protruding hemisphere, right column in Figure 9. It suggests that the necklace vortex gets weaker with the decreasing height of the turret due to a less-blockage effect from the turret. Spatial distribution of OPDrms is very similar for the flat-aperture and the conformal-aperture turrets at this azimuthal angle.

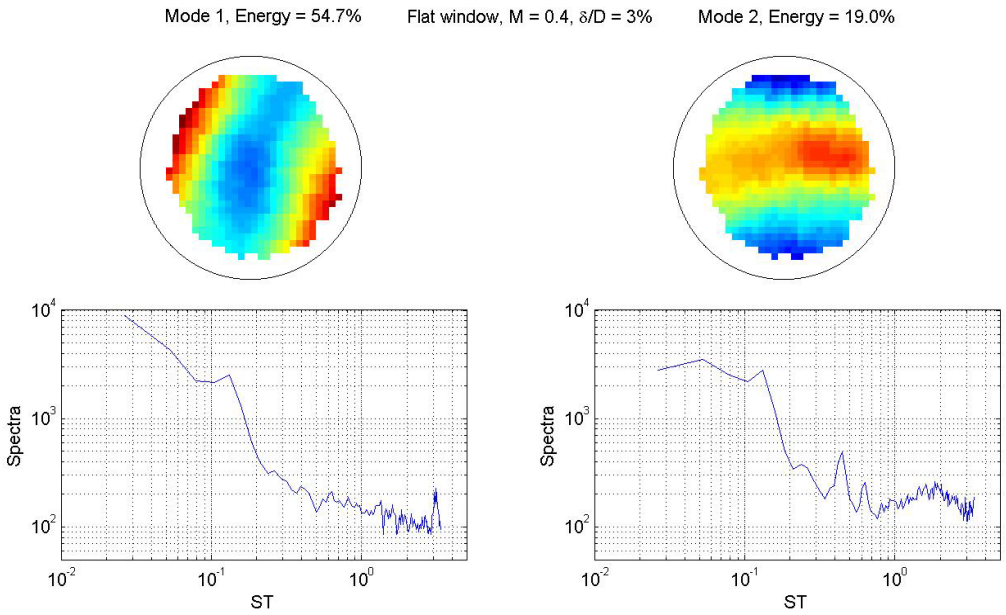

Figure 8. Top: First two dominant spatial POD modes for the full turret with the flat aperture, azimuthal angle is 0 degrees, M = 0.4, δ/D = 0.03. Bottom: spectra of the temporal coefficients for these POD modes.

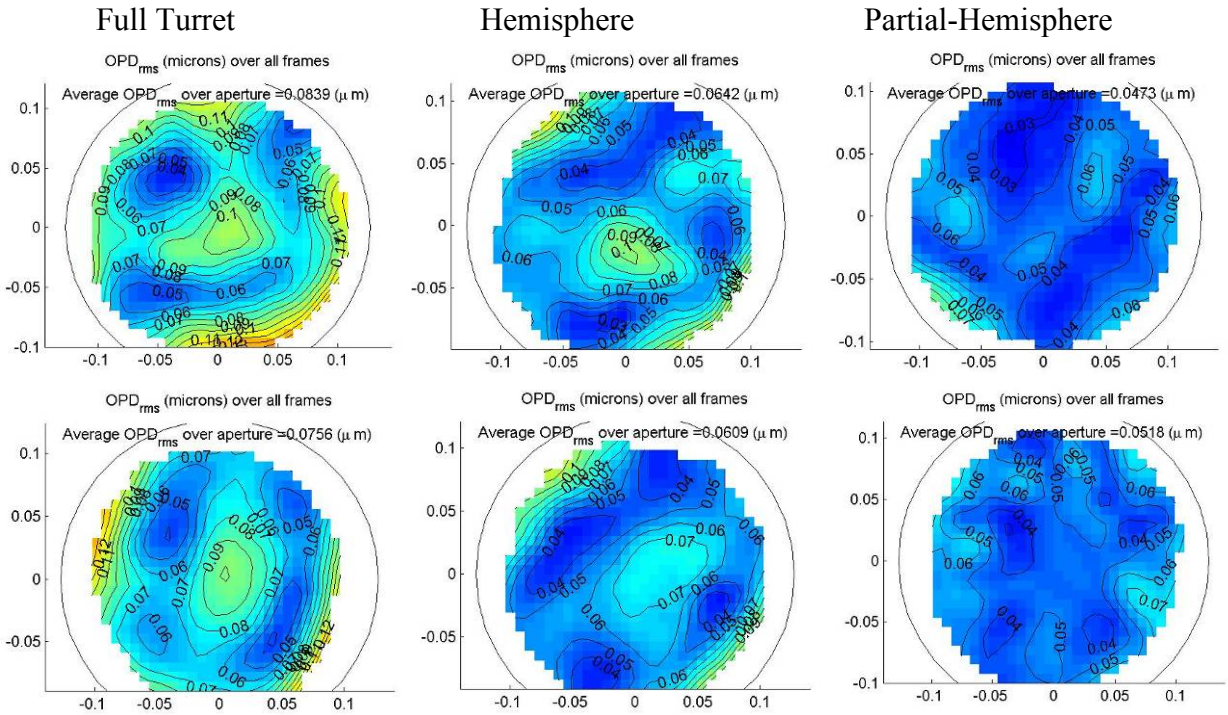

Figure 9. Spatial distribution of OPDrms for the conformal (top row) and flat-aperture (bottom row) turret for different heights. Azimuthal angle is 0 degrees, the incoming M = 0.4, δ/D = 0.03.

Spatial distribution of OPDrms for the side-looking azimuthal angle of 85 degrees for different aperture types and turret heights are shown in Figure 10. For the conformal-aperture turret, top row in Figure 10, the flow stays attached, and the small peak in the spatial distribution of OPDrms near the aperture suggests that the most of the aero-optical distortions are from the unsteady defocus due the slow variation in the necklace vortex. For the flat-aperture turret, bottom row in Figure 10, a slope discontinuity at the leading edge of the aperture trips and energizes the boundary layer, which consequently leads to an increase in overall OPDrms at this angle, compared to the

conformal-aperture turret. OPDrms level drops for the hemisphere and then rises for the partial hemisphere. It might be contributed at an increased interaction of the tripped boundary layer and the necklace vortex, which is located near the bottom of the aperture for the partial hemisphere.

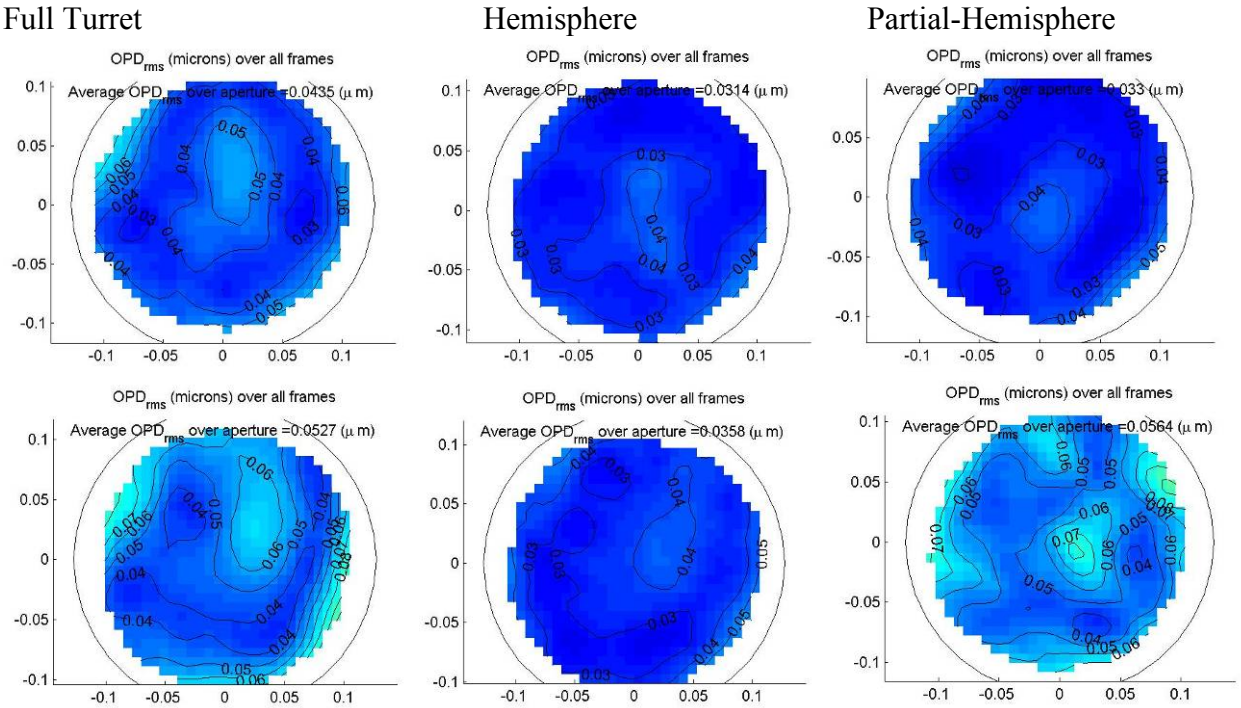

Figure 10. Spatial distribution of OPDrms for the conformal (top row) and flat-aperture (bottom row) turret for different heights. Azimuthal angle is 85 degrees, the incoming M = 0.4, δ/D = 0.03.

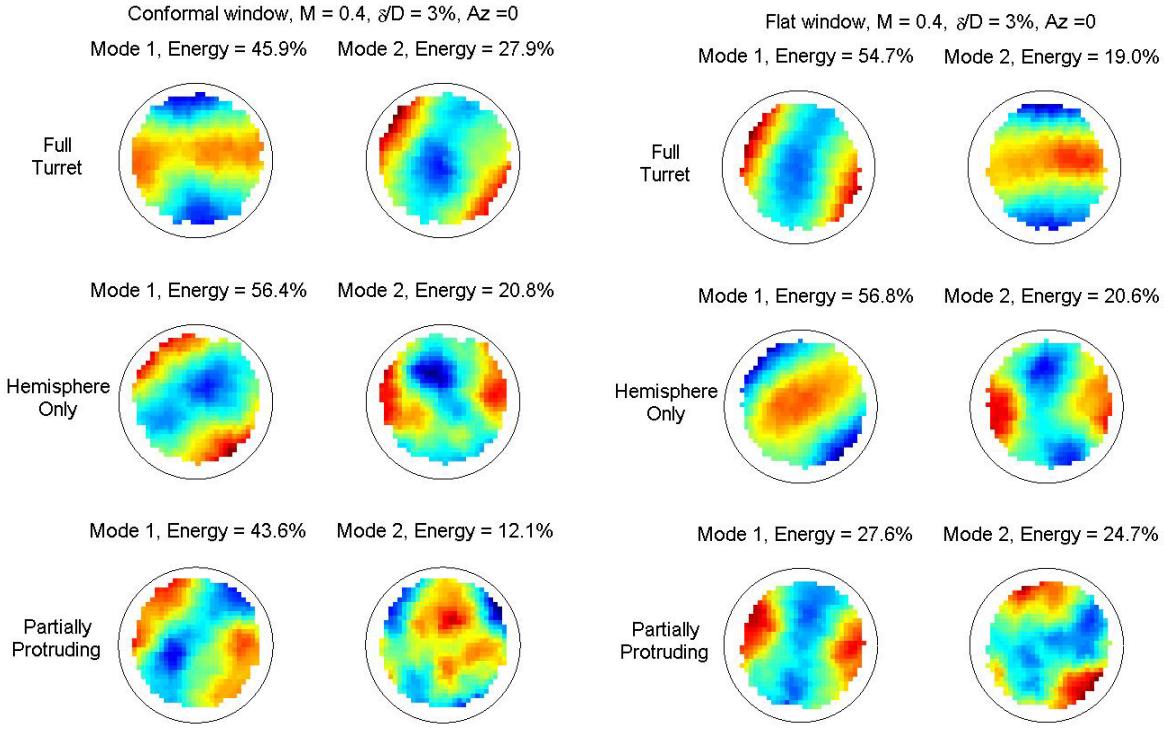

Figure 11. First two POD modes for a conformal window turret (left) and a flat window turret (right) for varying turret heights at Az = 0, M = 0.4, and δ/D = 0.03.

The dominant POD modes at the azimuthal angle of 0 degrees exhibit a dependence on turret height, as shown in Figure 11. Moving from a full turret to the hemispherical turret, the previously discussed mode differences between the flat and conformal windows disappears. Both geometries have very similar dominant modes and energy content; at this height, the flat window has little to no effect on the dominant aberrating modes. The mode shapes change from the horizontal and vertical defocus modes to a defocus at an angle of approximately 45° and a mode that appears similar to an astigmatism mode. A possible explanation for this shift is that the slow changes of the wake and necklace vortex that drive the defocus for the full turret changes dynamics with the smaller wake and altered the necklace vortex present on the hemispherical turret. A further shift is observed moving to the partial turret; the primary mode for both remains a defocus mode, but the mode is significantly more energetic for the conformal window than for the flat window. The second modes are different between the two windows as well, in both shape and energy content. A potential explanation for this case is that the flat window is now low enough to possibly interact with the necklace vortex or the incoming boundary layer, modifying the defocus.

B. Effect of Incoming BL thickness

The results of the incoming BL thickness on aero-optical distortions for the full turret with the conformal and flat apertures are presented in Figure 12. For the full turret and the hemisphere only, the incoming BL thickness has a small effect of aero-optical distortions, with the exception of the azimuthal angle of 0 degrees for the full turret with a flat aperture, where OPDrms increases for the thick BL, as seen in upper right plot in Figure 12. In fact, for the forward-looking angle of zero degrees, BL thickness does not have a clear trend on OPDrms, see Figure 10, upper plot. For instance, for the full and hemispherical turrets, OPDrms slightly drops for the medium BL thickness, but it goes up, although not by much, for the thick boundary layer; the same time, OPDrms for the partially-protruding hemisphere shows the opposite trends.

The BL thickness primarily affects the level of aero-optical distortions for the partially-protruding turret, increasing OPDrms levels with increasing BL thickness. For the partially-protruding turret, the aperture is located near the tunnel wall, see Figure 4, right, where the necklace vortex is formed; therefore, the necklace vortex is located near the bottom of the aperture, thus directly affecting aero-optical distortions. The thickness of the incoming BL affects the vortex strength and therefore, related aero-optical aberrations. For the conformal-aperture turret, and, at a lesser degree, for the flat-aperture turret, the aero-optical distortions around the partially-protruding hemisphere increase monotonically, although weakly, with the incoming BL thickness for the azimuthal angle of 45 degrees, see Figure 10, middle plots. BL thickness has the smallest effect for the side-looking angle of 85 degrees for both the conformal- and the flat-aperture turrets, see bottom plots in Figure 12.

As mentioned before, aero-optical distortions have non-monotonic trends with the incoming boundary layer thickness for the forward-looking angle. Spatial distributions of OPDrms for the flat-aperture turret at full height and the partially-protruding hemisphere for the forward-looking azimuthal angle of 0 degrees for different incoming boundary layers are presented in Figure 13. For the full turret, upper row in Figure 13, the unsteady defocus is clearly a main contributor the overall OPDrms and OPDrms is the largest for the thick boundary layer. As mentioned before, for the partially-protruding hemisphere, bottom row in Figure 13, the necklace vortex is formed at the bottom of the turret with its size increasing with the incoming boundary layer thickness. Therefore, the initial trend for OPDrms is to increase with the incoming boundary layer. However, for the large incoming boundary layer, its size becomes comparable with the turret height. For the partial-hemisphere it is 40% of the turret height and for such thick boundary layer the necklace vortex might engulf the whole turret. In this case OPDrms near the aperture will be affected only by a portion of the vortex, which leads to a drop in OPDrms for large incoming boundary layers.

Keep in mind that the above explanation is only one possible explanation, based on analysis of aero-optical data only. Additional measurements, including instantaneous vortex dynamics and aero-optical measurements, should be performed to better understand these trends for the azimuthal angle of 0 degrees.

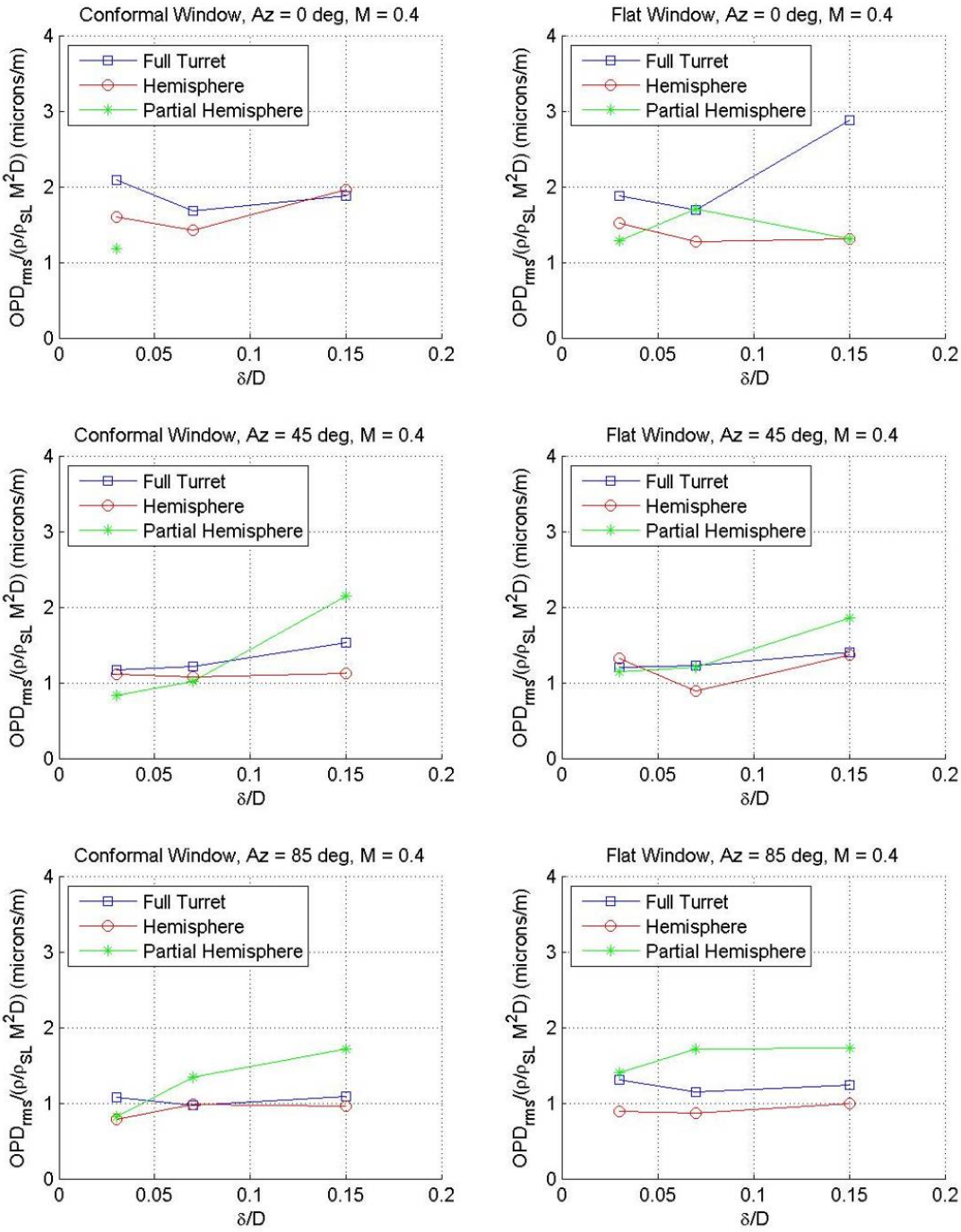

Figure 12. Effect of the incoming BL thickness on normalized OPDrms for the turret with conformal (left column) and flat (right column) apertures as a function of the incoming BL thickness for the azimuthal angle of 0 (upper row), 45 (middle row) and 85 degrees (bottom row). The incoming M = 0.4.

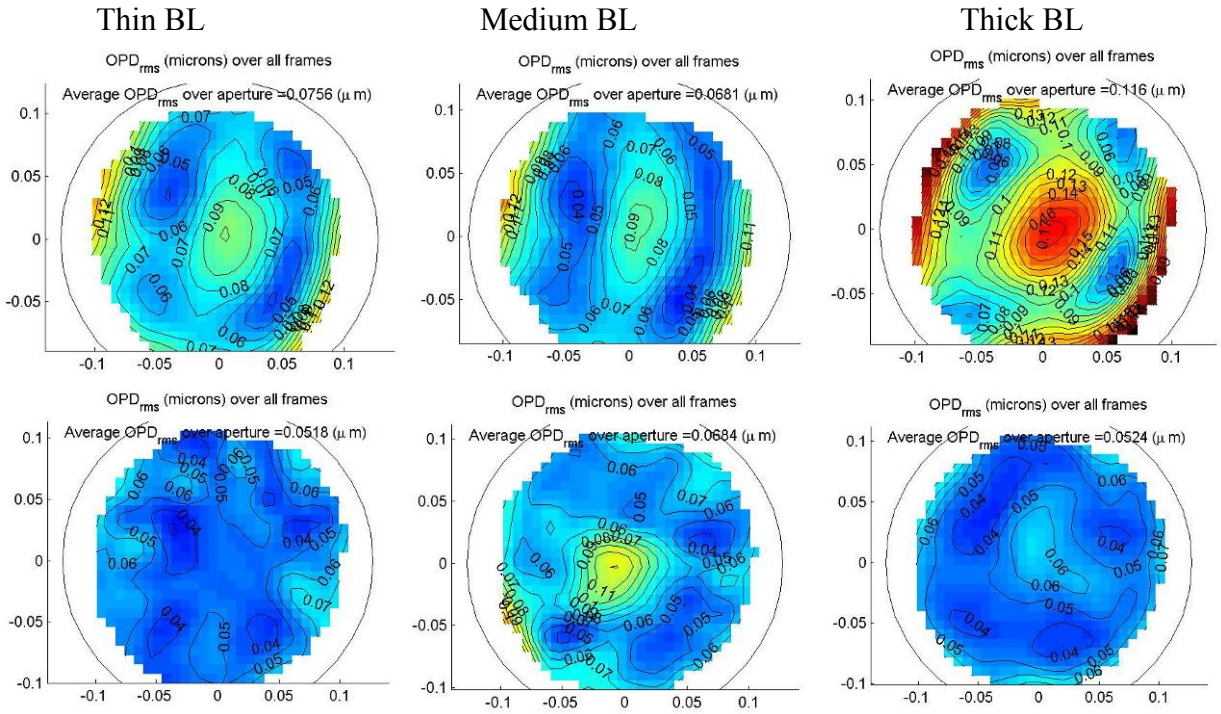

Figure 13. Spatial distribution of OPDrms for the flat-aperture turret, the full turret (top row) and the partial hemisphere (bottom row) turret for different incoming BL thicknesses. Azimuthal angle is 0 degrees, the incoming M = 0.4.

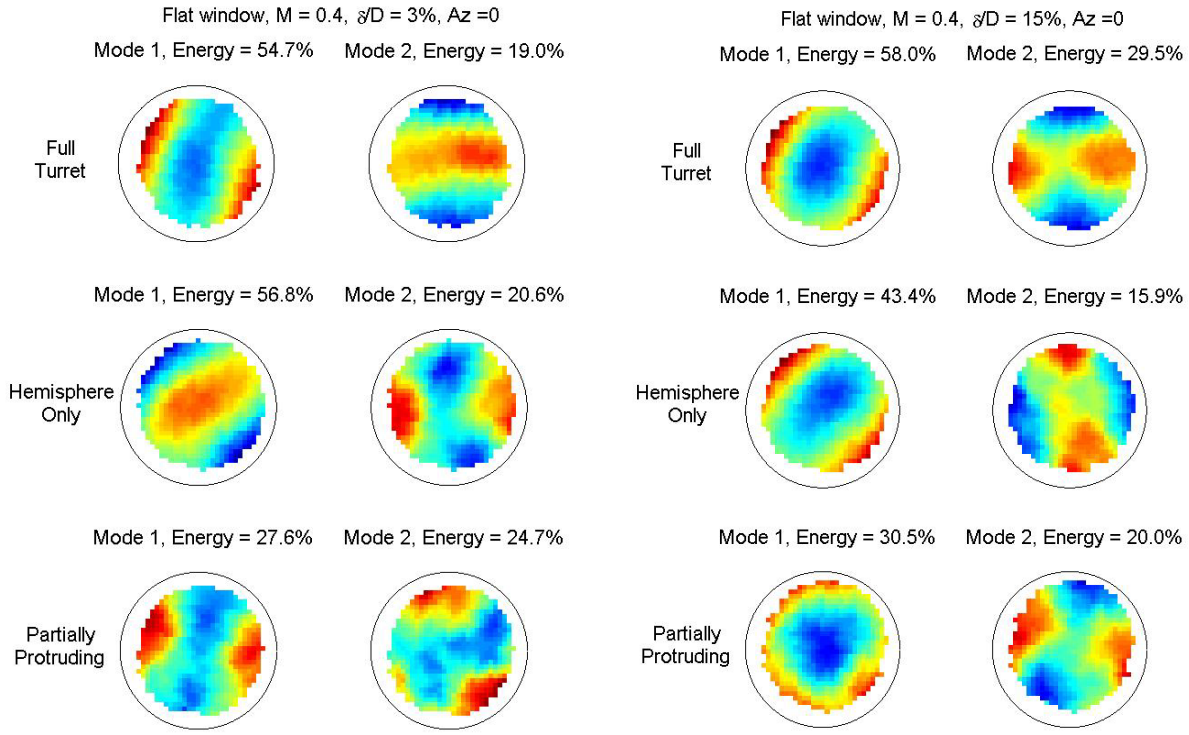

Figure 14. Comparison of POD modes and energies for a flat window turret at Az = 0°, M = 0.4 for varying turret heights at δ/D = 0.03, left and δ/D = 0.15, right.

Figure 14 shows the dominant POD modes and energies for the flat window turret as turret height varies for the thinnest and thickest boundary layer. The first mode of the full turret experiences very little change when the boundary layer size is increased, with the horizontal defocus becoming closer to a spherical defocus and the energy content increases by about 3%. The second mode for the full turret, however, greatly increases in energy content and changes from the vertical defocus to an astigmatism mode. This astigmatism mode is present as the second most contributing mode for all three heights at the thickest boundary layer. This shows that the increased boundary layer still has an effect on the turret's necklace vortex for the full turret, which impacts the unsteady defocus. The hemispherical turret shows a similar pattern of the primary defocus mode approaching a spherical defocus from a linear defocus. However, both of the modes for this height have an energy reduction compared to the thin boundary layer—for the hemispherical turret, the increased boundary layer height has the effect of reducing the total amount of order observed in the wavefronts. For the partial hemisphere, when the BL thickness is increased, the first horizontal defocus mode becomes a purely spherical defocus, while the second mode becomes the astigmatism mode observed at the other two heights. For this turret height, the sum total energy content between the first two modes is unchanged, but the first mode is slightly more energetic for the larger boundary layer, indicating a stronger defocus as well as a reshaped one.

C. Mach number dependence

OPDrms, normalized by the turret diameter, D, over the aperture for a range of Mach numbers between 0.3 and 0.6 for the partially-protruding hemisphere with either the conformal- or the flat-aperture for all azimuthal angles for the thin incoming BL are presented in Figure 15 as a function of $\rho/\rho_{SL}M^2$. If OPDrms/D is linearly proportional to $\rho/\rho_{SL}M^2$, it suggests the Re-number independence of the underlying flow physics [1]. For the conformal-aperture turret at the azimuthal angle of 45 degrees, see left plot in Figure 15, OPDrms/D is indeed linear with $\rho/\rho_{SL}M^2$, except for M = 0.3; at this relatively-low speed transient effects around the turret might play a role, as suggested in other related turret studies [1]. For the azimuthal angle of 85 degrees, the trend is also linear, except for M = 0.6, where an intermittent supersonic shock appears over the aperture, leading to an additional increase in OPDrms. For the flat-aperture turret, see right plot in Figure 15, the shock is anchored at the downstream slope discontinuity, keeping the flow subsonic over the aperture. As a result, OPDrms is approximately proportional to $\rho/\rho_{SL}M^2$ over the whole range of Mach numbers at azimuthal angles of 45 and 85 degrees, again with the exception of the low M = 0.3. However, at the azimuthal angle of zero degrees, OPDrms/D is not linear with $\rho/\rho_{SL}M^2$ for both apertures, suggesting that the dynamics of the necklace vortex, which is a predominant aero-optical source at this angle, has a weak Re-number dependence.

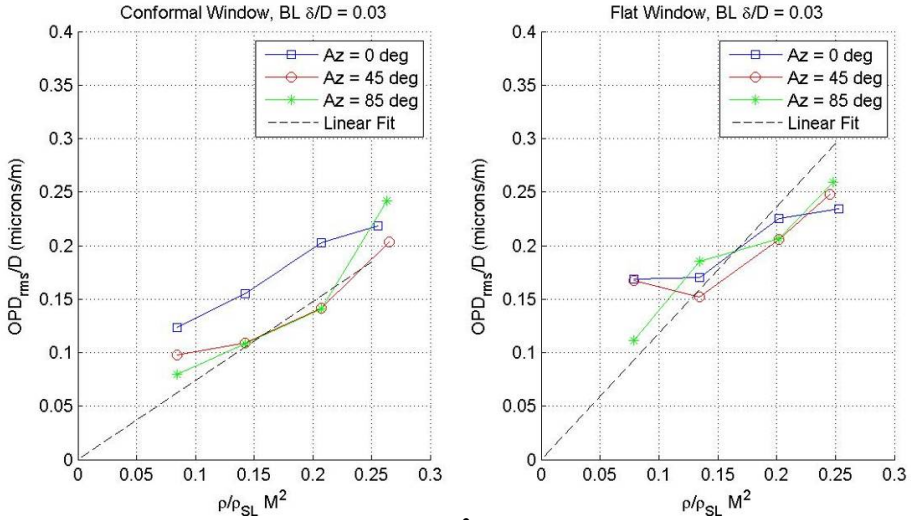

Figure 15. OPDrms, normalized by D versus $\rho/\rho_{SL}M^2$ for the partially-protruding hemisphere for the thin incoming BL.

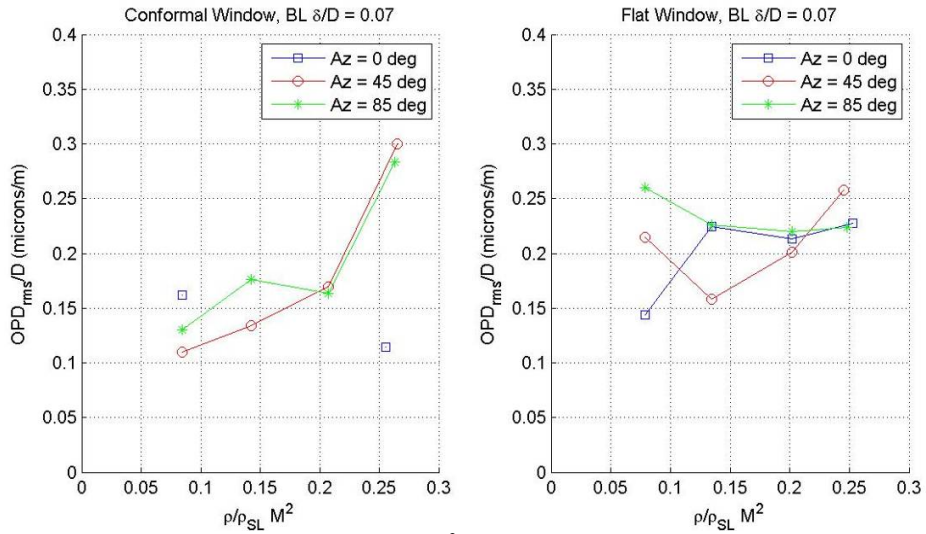

Figure 16. OPDrms, normalized by D versus $\rho/\rho_{SL}M^2$ for the partially-protruding hemisphere for the medium incoming BL.

As discussed in the previous section, a large incoming boundary layer significantly modifies the formation and the dynamics of the necklace vortex around the partially-protruding hemisphere. The Mach-number dependence of OPDrms/*D* for the medium incoming boundary layer of δ/D = 0.07, or 20% of the turret height, is presented in Figure 16. While overall levels of OPDrms for the conformal-aperture turret have a somewhat monotonic trend with the increasing Mach number for the azimuthal angles of 45 and 85 degrees, aero-optical distortions for the flat-aperture turret show more complex trends, showing transient effects for low M = 0.3 and even independence of the Mach number for the range of M between 0.4 and 0.6 for the azimuthal angles of 0 and 85 degrees. Additional simultaneous fluidic and aero-optical measurements are required for a better understanding of the physics of aero-optical distortions around partially-protruding hemispheres for large incoming boundary layers.

V. Global Jitter Results

Jitter spectra for the azimuthal angle of 0 degrees for M = 0.4 are presented in Figure 17 for different turret heights and apertures. Most of the jitter is located at low, less that ST = 2, frequencies, with one "hump" at ST = 0.13, and the second 'hump" at ST = 0.2; the second peak appears to be slightly narrower for flat-aperture turrets. These spectra shapes are very similar to the spectra for the unsteady defocus observed in Figure 7, bottom plots, also suggesting the link between the necklace vortex dynamics and aero-optical distortions, including the global jitter. Similar to trends for overall levels of aero-optical distortions, observed in Figure 6, the spectra amplitude almost monotonically increase with the turret height, as the partially-protruding hemisphere has the least amount of jitter and the full turret has the largest jitter over a wide range of frequencies. For ST > 0.3 at these angles, the jitter is likely driven by the necklace vortex, and as the turret height get reduced, the weaker necklace vortex has less impact on the global jitter.

For the azimuthal angle of 85 degrees, the spectra shapes look similar, see Figure 18; the "hump" at ST = 0.13 is less pronounced for the flat-aperture turret. The full turret also produces the strongest jitter spectrum, while differences between the jitter spectra between the hemisphere and the partially-protruding hemisphere are fairly small.

Effect of the BL thickness on the global jitter for the full turret at the azimuthal angle of zero degrees is shown in Figure 19. The effect is rather small, with the thick BL producing a slightly-stronger jitter spectrum, compared to the jitter spectra for the thin and the medium BL; the spectra for last two BL thicknesses virtually overlap. For the partially-protruding hemisphere, see Figure 20, the thick BL also creates a stronger jitter spectrum, compared to the medium and the thin BL, especially in the range of ST between 0.5 and 2.

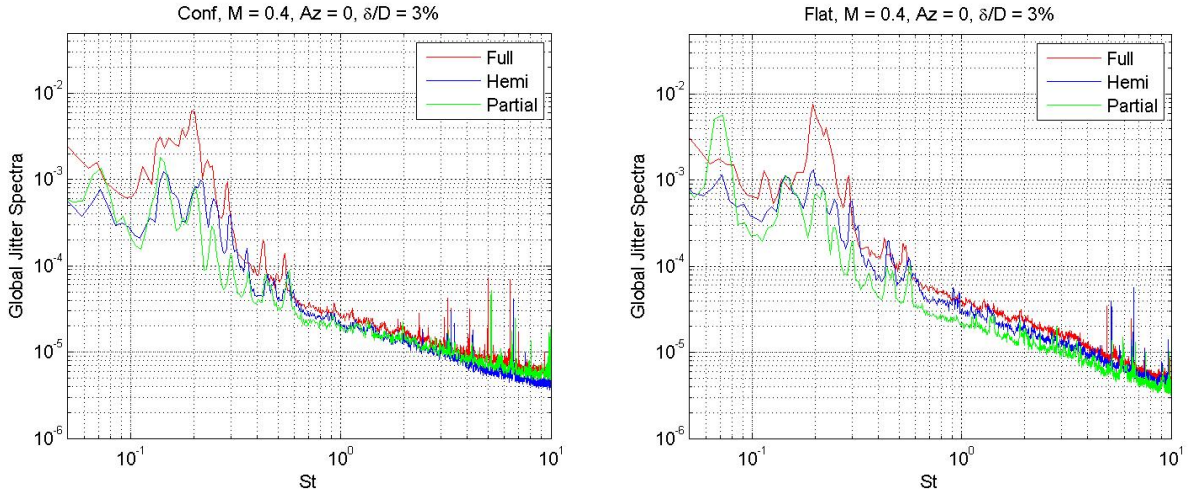

Figure 17. Global jitter spectra for different turret heights with conformal (left plot) and flat (right plot) apertures at the azimuthal angle of 0 degrees. The incoming M = 0.4.

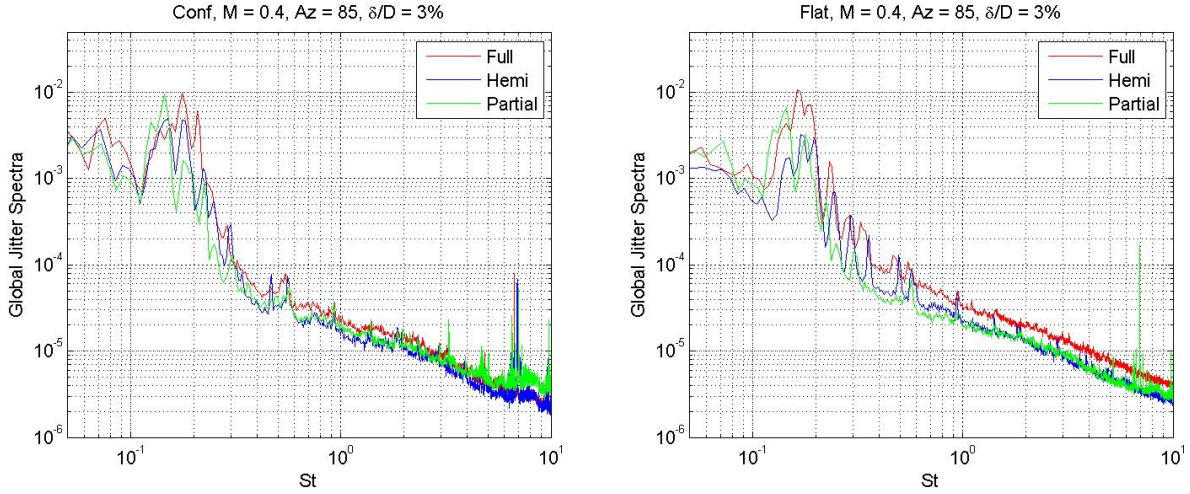

Figure 18. Global jitter spectra for different turret heights with conformal (left plot) and flat (right plot) apertures at the azimuthal angle of 85 degrees. The incoming M = 0.4.

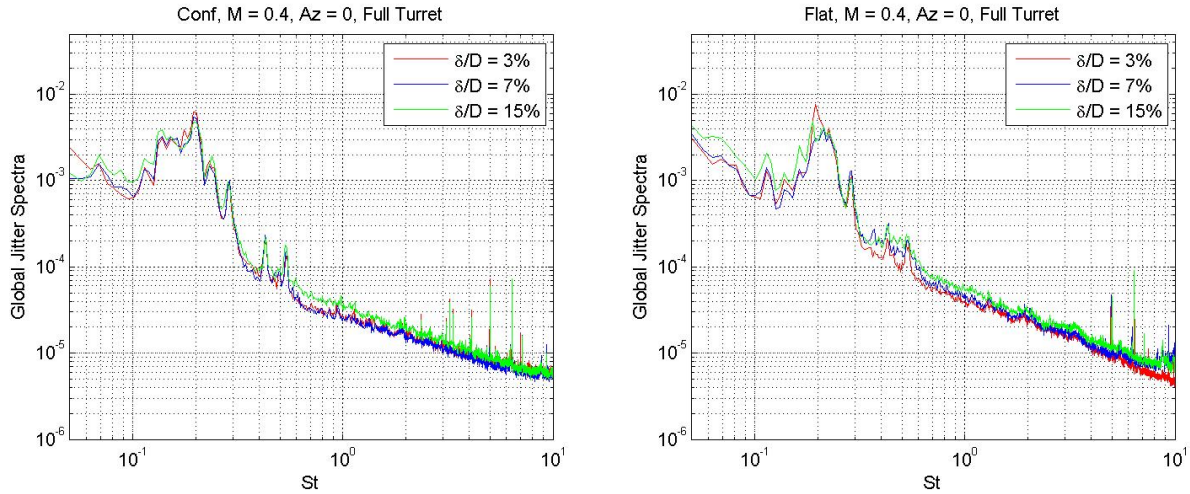

Figure 19. Global jitter spectra for different incoming BL thicknesses for the full turret with conformal (left plot) and flat (right plot) apertures at the azimuthal angle of 0 degrees. The incoming M = 0.4.

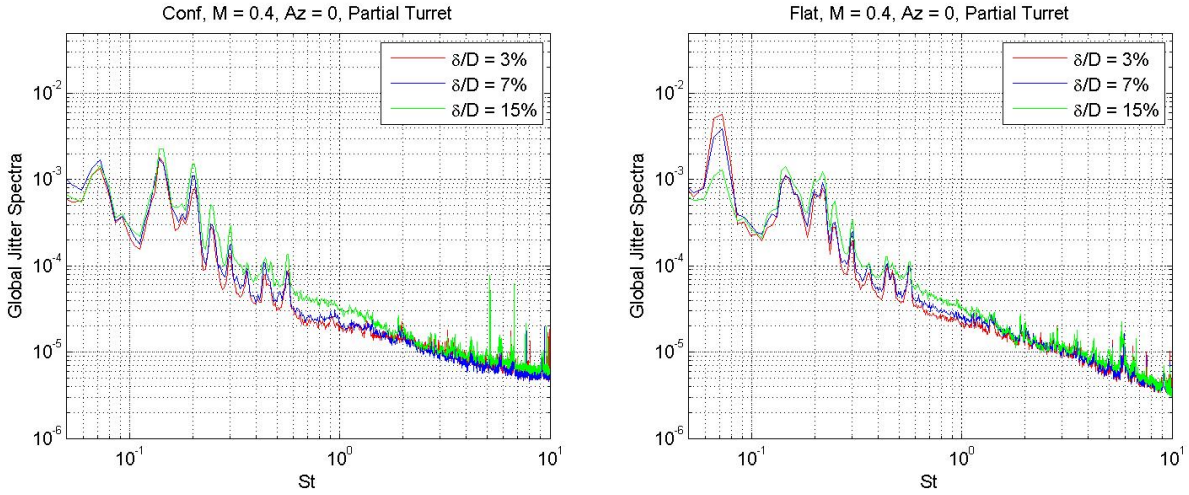

Figure 20. Global jitter spectra for different incoming BL thicknesses for the partially-protruding hemisphere with conformal (left plot) and flat (right plot) apertures at the azimuthal angle of 0 degrees. The incoming M = 0.4.

For the full turret at the azimuthal angle of 85 degrees, the incoming BL thickness has a very small effect on the jitter spectra, as seen in Figure 21. For the partially-protruding hemisphere, see Figure 22. The BL thickness effect is small for the thin and the medium BL thickness, but the thick BL significantly increases the jitter spectrum for ST between 0.4 and 3. Most likely, this increase is related to the increased strength and, possibly different dynamics of the necklace vortex, located at the bottom of the aperture and directly influencing the beam jitter. As the aperture is located close enough to the floor of the tunnel for necklace vortex to lie directly in the beam path, as can be seen in figure 5, it's possible that the boundary layer is forcing the necklace vortex to be unstable. The instability of the necklace vortex, coupled with its size due to the increased boundary layer thickness would introduce additional global tilt on the wavefront. This trend is consistent with similar conclusions about the effect of the large boundary layers on higher-order aero-optical distortions, discussed earlier.

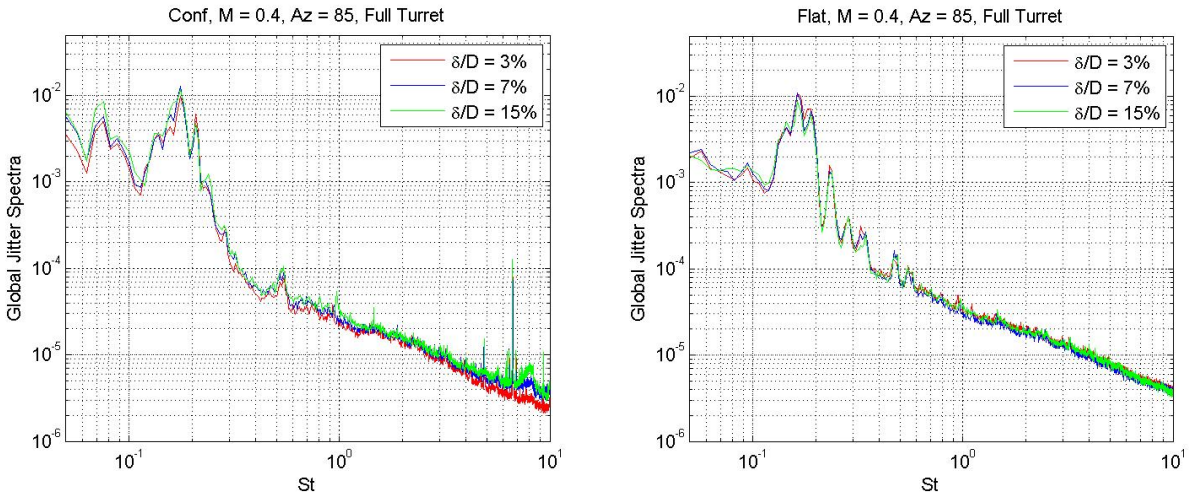

Figure 21. Global jitter spectra for different incoming BL thicknesses for the full turret with conformal (left plot) and flat (right plot) apertures at the azimuthal angle of 85 degrees. The incoming M = 0.4.

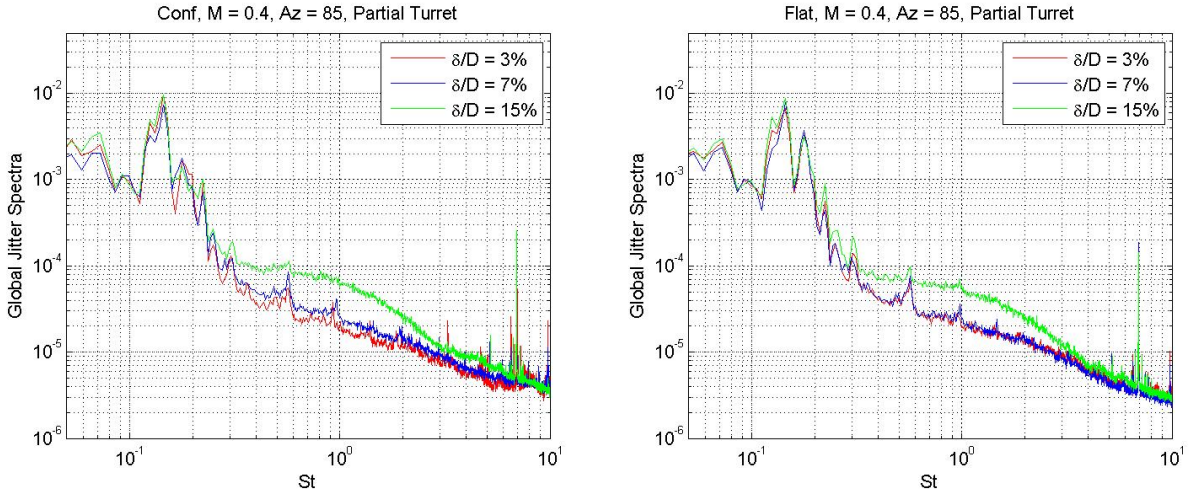

Figure 22. Global jitter spectra for different incoming BL thicknesses for the partially-protruding hemisphere with conformal (left plot) and flat (right plot) apertures at the azimuthal angle of 85 degrees. The incoming M = 0.4.

VI. Conclusions

Extensive optical measurements of the aero-optical environment around turrets of different heights and aperture geometries were conducted for three forward-looking angles and several subsonic Mach numbers between 0.3 and 0.6. Also, the effect of the incoming boundary layer was extensively experimentally studied by tripping and thickening the incoming boundary layer. Time-resolved wavefronts and global jitter data were collected for all cases. Results showed that for a thin incoming boundary layer the full-height turret has a largest level of aero-optical distortions, and the partially-protruding hemisphere has the lowest amount of distortions. Somewhat unexpectedly, aero-optical distortions at looking-straight-forward angle were larger than the aero-optical distortions at side-looking angles. Analysis of the temporal dynamics of wavefronts using POD revealed that these aberrations are dominated by slow-varying defocus. It was hypothesized that these low-frequency variations are due to the slow variation in the topology of the necklace vortex at the bottom of the turret. The effect of the incoming boundary layer thickness was generally to slightly increase aero-optical aberrations, but in some cases trends were different for different turret heights, aperture geometries and azimuthal angles. It was especially clear for the partially-protruding hemispherical turret and the incoming boundary layer at 40% of the turret height, where the thick boundary layer significantly changed the topology and dynamics of the necklace vortex and resulted aero-optical distortions.

Additional POD analysis shows that the shape of the defocus mode depends not only on the turret geometry but also the incoming boundary layer thickness. The flat and conformal windows are dominated by opposite-orientation defocus modes for the full turret, a difference that disappears for the hemisphere-only and partially-protruding hemisphere turrets. The shape of the defocus changes as the boundary layer increases to $\delta/D = 0.15$, switching from a linear defocus across the aperture to a more spherical shape for both the full turret and the hemisphere-only turret; while for the partially-protruding hemisphere, the defocus becomes fully spherical. All three turret heights also had an astigmatism shaped mode as the second most energetic mode. As these defocus effects are likely due to perturbations in the necklace vortex and the wake, this shows that the incoming boundary layer height has a direct effect on the magnitude and shape of those perturbations.

Analysis of the global jitter also suggested that the dynamics of the necklace vortex affects the beam jitter and, in general, the global jitter data have very similar trends observed in higher-order wavefront data. For the largest boundary layer, a hump appears in the partial hemisphere global jitter spectra between ST = 0.4 and ST = 3. This hump is likely due to increased size and unsteadiness of the necklace vortex, which is located directly in the beam path for this height.

Future work will focus on augmenting optical measurements with additional fluidic measurements to study the exact cause and parametric evolution of the source of the unsteady defocus. To this end, simultaneous PIV and wavefront measurements will allow correlation between necklace vortex perturbations and the defocus component present in the wavefronts. Additionally, further investigation into the effect of the boundary layer thickness on turrets of varying geometry, especially in regard to necklace vortex dynamics would prove useful in explaining these optical results.

Acknowledgments

This work was funded by the Air Force Research Laboratory, Directed Energy Directorate. The U.S. Government is authorized to reproduce and distribute reprints for governmental purposes notwithstanding any copyright notation thereon.

References

[1] S. Gordeyev and E. Jumper, "Fluid Dynamics and Aero-Optics of Turrets", *Progress in Aerospace Sciences*, **46**, (2010), pp. 388-400.

[2] M. Weng, A.Mani and S. Gordeyev, "Physics and Computation of Aero-Optics", *Annual Review of Fluid Mechanics*, Vol. **44**, pp. 299-321, 2012.

[3] C. Porter, S.Gordeyev, M. Zenk and E. Jumper, "Flight Measurements of Aero Optical Distortions from a Flat-Windowed Turret on the Airborne Aero-Optics Laboratory (AAOL)", AIAA Paper 2011-3280, 2011.

[4] N. De Lucca, S. Gordeyev and E. Jumper, "The Airborne Aero-Optics Laboratory, Recent Data", Acquisition, Tracking, Pointing, and Laser Systems Technologies XXVI, Proceedings of SPIE, Volume 8395, Paper 8395-7, June, 2012.

[5] B. Vukasinovic, A. Glezer, S.Gordeyev, E. Jumper and V. Kibens, "Hybrid Control of a Turret Wake," *AIAA Journal*, Vol. **49**, No. 6, pp. 1240-1255, 2011.

[6] M. Palaviccini, L. Cattafesta and B. George," Passive Flow Control over a Three-Dimensional Turret with a Flat Aperture", AIAA Paper 2011-3265, 2011.

[7] R. Jelic, S. Sherer and R.Greendyke, "Simulation of Various Turret Configurations at Subsonic and Transonic Flight Conditions Using OVERFLOW", AIAA Paper 2012-464, 2012.

[8] N. De Lucca, S. Gordeyev and E. Jumper, "The Study of Aero-Optical and Mechanical Jitter for Flat Window Turrets ", AIAA Paper 2012-0623.

[9] N. De Lucca, S. Gordeyev and E. Jumper, "Comparison of Aero-Optical Measurements from the Flight Test of Full and Hemispherical Turrets on the Airborne Aero-Optics Laboratory", 43nd AIAA Plasmadynamics and Lasers Conference, 25 - 28 June 2012, New Orleans, Lousiana, AIAA Paper 2012-2985

[10] S. Gordeyev, R. Burns, E. Jumper, S. Gogineni, M. Paul and D. J. Wittich," Aero-Optical Mitigation of Shocks Around Turrets at Transonic Speeds Using Passive Flow Control", 51st AIAA Aerospace Sciences Meeting , 7-10 Jan 2013, Grapevine, TX

[11] Goorskey, DJ, "Spatial And Temporal Characterization of AAOL Flight Test Data", Acquisition, Tracking, Pointing, and Laser Systems Technologies XXVI, Proceedings of SPIE, Volume **8395**, Paper 8395-8, June, 2012.

[12] Adrian, R.J., "On the role of conditional averages in turbulent theory", In: Turbulence in Liquids: Proceedings of the 4th Biennial Symposium on Turbulence in Liquids, ed. G. Patteson and J. Zakin, Science Press, Princeton, 1977, pp. 322-33